ACE: A fast, skillful learned global atmospheric model for climate prediction

Oliver Watt-Meyer,* **Gideon Dresdner, Jeremy McGibbon, Spencer K. Clark, Brian Henn, Matthew E. Peters, and Christopher S. Bretherton**
Allen Institute for Artificial Intelligence (AI2), Seattle, USA

James Duncan†
Graduate Group in Biostatistics, University of California, Berkeley USA

Noah D. Brenowitz, Karthik Kashinath, Michael S. Pritchard, and Boris Bonev
NVIDIA, Santa Clara, USA

Abstract

Existing ML-based atmospheric models are not suitable for climate prediction, which requires long-term stability and physical consistency. We present ACE (AI2 Climate Emulator), a 200M-parameter, autoregressive machine learning emulator of an existing comprehensive 100-km resolution global atmospheric model. The formulation of ACE allows evaluation of physical laws such as the conservation of mass and moisture. The emulator is stable for 100 years, nearly conserves column moisture without explicit constraints and faithfully reproduces the reference model's climate, outperforming a challenging baseline on over 90% of tracked variables. ACE requires nearly 100x less wall clock time and is 100x more energy efficient than the reference model using typically available resources. Without fine-tuning, ACE can stably generalize to a previously unseen historical sea surface temperature dataset.

1 Introduction

The last year has seen a revolution in the field of numerical weather prediction. Multiple groups have shown improvements in key metrics over the state of the art physics-based medium-range weather prediction system using deep learning methods [2, 5, 13]. However, the applicability of these methods to climate modeling is unclear. Nearly all machine learning based weather prediction systems [2, 5, 11, 13, 16] have reported results for forecasts up to only 14 days—with notable exceptions of [3, 23]—and instabilities or unphysical artifacts often occur for longer simulations.

We claim the requirements of an ML-based atmospheric model for climate prediction are as follows. Such a model should maintain realistic weather variability and be stable for indefinite periods. Conservation of mass, moisture and energy is key. Surface and top-of-atmosphere fluxes of energy, moisture and momentum must be predicted to enable assessment of climate sensitivity and coupling with other components such as the ocean. Appropriate forcings should be used—e.g. sea surface temperature (SST) in the case of an atmosphere-only model. Its long-term averages should be unbiased compared to a reference dataset. Finally, the model's performance must generalize across a broad range of plausible SST distributions and CO_2 concentrations.

---

*oliverwm@allenai.org
†2023 summer intern at AI2

Here we present ACE (AI2 Climate Emulator)[3], a neural network based atmospheric model which satisfies many of the criteria listed above. ACE uses the Spherical Fourier Neural Operator (SFNO) architecture [3] and is trained to emulate an existing physics-based atmospheric model with 6-hour temporal resolution. ACE runs stably for at least 100 years and can simulate a decade in one hour of wall clock time, nearly 100 times faster than the reference atmospheric model, while consuming 100 times less energy. ACE predicts diagnostics such as the fluxes of energy and moisture through the top of atmosphere and Earth surface (e.g. precipitation). The model is framed so that precise evaluation of conservation of mass and moisture is possible and we find that column moisture is very nearly conserved across individual timesteps. External forcings, such as incoming solar radiation and sea surface temperature, are used as inputs. Finally, ACE replicates the near-surface climatology of the reference model better and runs much faster than a 2x coarser but otherwise identical version of that model.

Related work includes ClimateBench [22] which proposes directly predicting climate metrics such as annual mean precipitation from input forcing variables like CO_2. The disadvantage of such an approach is the limited physical interpretability: for example what sub-annual variability gives rise to the annual mean? Another study [15] trains on climate model output but makes forecasts with 14- or 30-day lead times, leading to smooth predictions near the climatological mean (e.g. Fig. 20 of [15]).

2 Methods

2.1 Dataset

Most ML-based weather prediction systems have been trained on the ERA5 reanalysis dataset [10]. While appealing due to its relatively accurate representation of historical atmospheric conditions, reanalysis data has downsides for the development of machine learning based climate models: it has a limited number of samples restricted to the recent past; models trained on reanalysis may not be reliable for future climates [1, 6]; and analysis increment terms (adjustments from observations) have no clear physical interpretation [19]. Therefore, we generate training data with an existing global atmospheric model (FV3GFS, the atmospheric component of the United States weather model [20, 24]).

The training data are an 11-member initial condition ensemble of 10-year simulations (hereafter the "reference" simulation; 10 years is length after discarding 3-month spinup time) performed on NOAA/GFDL's GAEA computer. Ten ensemble members are used for training and the eleventh for validation. For simplicity, we use annually repeating climatological sea surface temperature (1982-2012 average) and fixed greenhouse gas and aerosol concentrations. The reference simulation has a cubed-sphere grid [17] with a horizontal spacing of about 100 km and 63 vertical layers. Model state is saved every 6 hours, with a combination of snapshot and interval-mean variables. See Table 1 for a complete description of variables used for training. For compatibility with SFNO we regrid conservatively from the cubed-sphere geometry of FV3GFS to a 1° Gaussian grid [21], additionally filtering the data with a spherical harmonic transform round-trip to remove artifacts in the high latitudes. We coarsen the vertical coordinate to 8 layers while conserving moisture and energy (Appendix A).

2.2 Training

Architecture We use the SFNO architecture [3] to predict the state of the atmosphere at time $t+6\mathrm{hr}$ using the state at time t as input. SFNO is a Fourier Neural Operator-based architecture which uses spherical harmonic transforms to enable efficient global convolutions on the sphere, while respecting inherent symmetries of the spherical domain. Hyperparameters are described in Appendix B; the number of parameters is about 200M. Unlike many prior ML atmospheric prediction systems, we use prognostic variables P which are both inputs and outputs, forcing variables F which are inputs only and diagnostic variables D which are outputs only (Table 1). Explicitly, with t representing the time index: $[P_{t+1}, D_{t+1}] = f(P_t, F_t)$, where f represents the SFNO module and forcing variables F_t are read from an external dataset (Figure 5). Variables are chosen to be forcing, prognostic or diagnostic based on how they are used in the reference physics-based simulation. The diagnostic variables do not inform the next step, which is typical for physics-based atmospheric models and has the important benefit that fields such as precipitation are not necessary to initialize a simulation. However, because

---

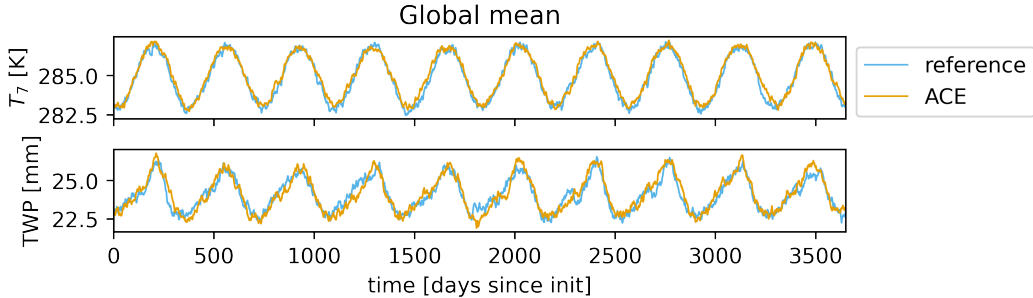[3]Code, data and model weights are publicly available; see https://github.com/ai2cm/ace.

Figure 1: Global mean timeseries of (top) near-surface air temperature T_7 and (bottom) total water path computed as $\text{TWP} = \frac{1}{g} \sum_k q_k^T \, dp_k$. For clarity, the daily average is plotted.

they are predicted by the same architecture that predicts the prognostic variables one can enforce physical constraints such as moisture conservation which affect prognostic model weights. This is different than some previous approaches which use a separate model to predict precipitation [16].

Data Normalization Variables are normalized using a "residual scaling" approach such that predicting outputs equal to input would result in each variable contributing equally to the loss function (similar to [11]). See Appendix H for details and Appendix I.1 for an ablation of this choice. This "residual scaling" approach has the largest impact on the surface pressure, which ends up having a normalized standard deviation about 20 times larger than otherwise (Figure 12).

Loss Function Given $\mathbf{x}_i$ representing the normalized target for the i'th sample of a batch for all spatial points and channels, and $\hat{\mathbf{x}}_i$ as the corresponding prediction, the loss for a batch of size B is $\frac{1}{B} \sum_{i=1}^{B} \frac{\|\hat{\mathbf{x}}_i - \mathbf{x}_i\|_2}{\|\mathbf{x}_i\|_2}$. The loss is computed after a single 6-hour forward step. Optimization hyperparameters are listed in Table 4.

2.3 Evaluation

We are not aware of any existing purely machine learning based system that allows for long (at least 10-year) forecasts and includes a vertically resolved view of the entire atmosphere. Therefore, we formulate baselines using our physics-based model. Two cases will be considered: first a "reference" perfect emulator in which we compare members of the initial condition ensemble against each other, giving an upper bound on model skill. Because of the chaotic nature of the atmosphere and the limited duration (10 years) of our validation dataset, even a perfect emulator will have non-zero errors. Second, we run a difficult-to-beat 200 km "baseline": the same physics-based FV3GFS model but using both horizontal resolution and dynamics time step that are 2x coarser. This mimics the typical climate modeling strategy for faster simulation: use coarser resolution at the cost of accuracy.

Three metrics are used for evaluation: the time-dependent area-weighted global mean and the area-weighted global mean bias and RMSE of time-mean fields. These are defined in Appendix C.

2.4 Random seed ensemble

Because long-term climate skill is not entirely constrained by the 6-hour prediction that is our training objective, we train an ensemble of 5 models which vary only in terms of their initialization random seed. Although validation loss is very similar between the models and all models are capable of stable 10-year forecasts, the magnitude of climate biases varies by up to a factor of 4 (depending on output variable). Hereafter, we report results for the model which performs best on the time-mean RMSE metric for T_7 and total water path (TWP) computed over a single 10-year forecast (see Figure 6).

3 Results

Long-term stability Initializing from the start of the validation dataset, ACE is able to maintain a stable simulation and an unbiased global mean evolution of temperature and total water path for
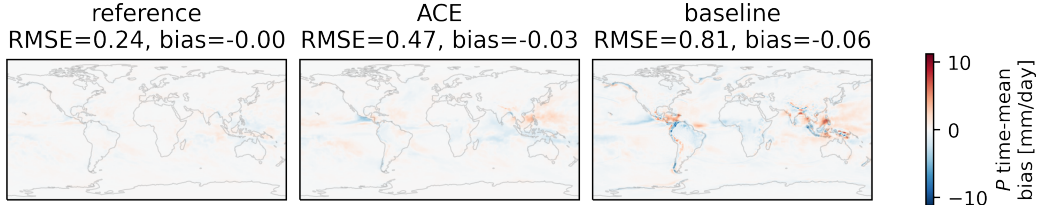
Figure 2: 10-year mean bias in surface precipitation rate. Titles show global and time-mean RMSE and bias in units of mm/day (Equations 6 and 7).
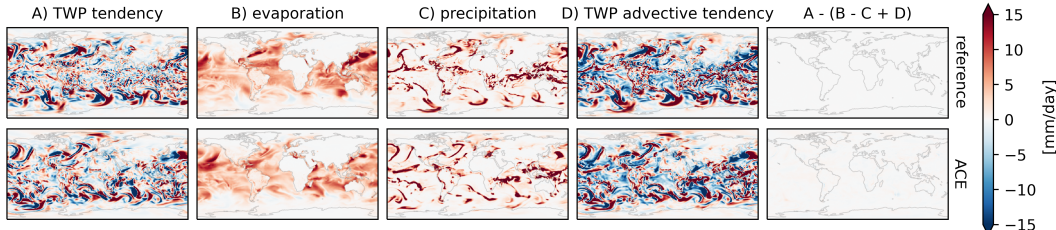

Figure 3: Snapshot of the terms in the column moisture budget (Equation 1) one year into simulation for (top) reference data and (bottom) ACE simulation. Given chaotic nature of atmosphere, we do not expect details to match between the reference and ACE simulations. If column-integrated moisture is exactly conserved, the rightmost column should equal zero, as it is for the reference data.

at least 10 years (Figure 1). While there is some year-to-year variability, the seasonal cycle of both of these fields is well represented by ACE. This result is dependent on choice of forcing variables, the normalization strategy (Appendix H) and using the SFNO architecture which has been shown to have favorable stability properties compared to Fourier Transform-based FourCastNet [3]. The two prognostic variables whose global means drift unrealistically are the surface pressure p_s and upper-stratospheric water q_0^T (Figure 9). This run has been extended to 100 years with no sign of instability or long-term drift (Figure 10). However, there are unrealistically large annual variations in certain fields, such as global mean precipitation rate.

Climate biases With long-term stability comes the possibility of quantitatively evaluating climate biases. Figure 2 shows the time-averaged bias in the spatial pattern of surface precipitation rate. ACE has impressively small precipitation biases, with a global RMSE about 42% smaller than the baseline. The time-mean biases and RMSEs are shown for all output channels in Appendix E. 41 out of 44 output variables have a lower time-mean RMSE for ACE compared to the baseline (Figure 7).

Physical consistency Many aspects of physical consistency are important for interpretability in climate model simulations. Here we discuss one example, the conservation of water expressed in terms of total water path:

$$\frac{\partial TWP}{\partial t} = E - P + \left.\frac{\partial TWP}{\partial t}\right|_{adv} \tag{1}$$

where $TWP = \frac{1}{g}\sum_k q_k^T dp_k$ is the amount of water in an atmospheric column and $\left.\frac{\partial TWP}{\partial t}\right|_{adv}$ is the tendency of the total water path due to advection. E and P are the surface evaporation and precipitation rate respectively ($E = LHF/L_v$). The physical model exactly satisfies Equation 1 by design but an ML emulator may not unless explicitly designed to do so. Nonetheless, ACE very nearly obeys the column-wise conservation of moisture (Eq. 1). Figure 3 shows the magnitude of the violation of the budget is very small compared to the individual terms in the budget: standard deviation of total water path tendency is ∼50 times that of the column budget violation term. This is true even one year into the inference simulation. Global mean budgets are described in Appendix G.

Zero-shot generalization to realistic sea surface temperature forcing In this work, as a first effort, we chose to train on a simplified dataset with annually repeating climatological SST. However,
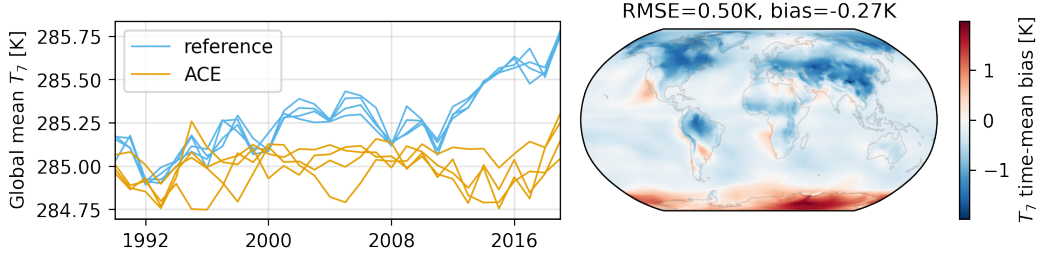
Figure 4: ACE forced with a realistic SST dataset spanning 1990-2020. Showing (left) timeseries of annual mean and global mean T_7, with individual lines corresponding to different initial conditions and (right) time-mean bias of T_7 for a single initial condition with time-mean RMSE and global bias (Equations 6 and 7) reported in the title. Here, the "reference" is the physics based model (FV3GFS) run for the same period and forced by the same SST pattern.

to be useful as a climate model, ACE must be skillful when forced by a wider variety of more realistic SST patterns. In this section we show results of zero-shot generalization to a forcing dataset with historical SSTs from 1990 to 2020 (using CMIP forcing data [8]). ACE is stable over the full 30-year span of this previously unseen forcing dataset (Figure 4a). This is particularly impressive because the climatological SST used to generate training data spans 1982-2012 and so the realistic SST dataset includes temperatures warmer than any in the training dataset. When forced with the realistic SST dataset, ACE has a cold near-surface temperature bias which is particularly amplified over land where the surface temperatures are not directly forced (Figure 4b) and it does not reproduce the interannual variability of the reference. The time-mean RMSE and bias of T_7 (0.5K and -0.27K, respectively) are somewhat larger than those when comparing ACE to a reference run which uses the climatological SST dataset (0.35K and 0.12K; see Figures 7 and 8). Nevertheless, the stability and modest biases of ACE when using this previously unseen SST dataset as a forcing are reassuring.

Computational expense   Training time for each seed was about 63 hours on four NVIDIA-A100s. Running inference on a single A100 requires about one second of wall clock time per simulated day. For comparison, the reference simulation ran on 96 cores of AMD EPYC 7H12 processors and took ∼77 seconds per simulated day. The 2x coarser resolution baseline ran on 24 cores in ∼45 seconds per simulated day.

4   Conclusions and future work

This work demonstrates the potential of deep learning for skillful and fast climate model emulation. 100x speed-up in run time and 100x greater energy efficiency could democratize the use of climate models, open new research avenues and potentially reduce energy usage. However, there are additional steps before this system is a useful climate model [8]. Generalizability is a key challenge. To reduce confounding factors, in this study we focused on a training dataset with simplified (annually-repeating) forcing. It may be necessary to expand the training and input variable set to be able to handle a changing climate. Our suggested approach is to train on a broad range of simulation data that covers the regimes of interest [6]. However, simulated data are not the real world and have their share of biases. Potential solutions are to fine-tune on reanalysis data (e.g. [9]) or on a smaller amount of high-resolution simulation data that has smaller biases [4]. Further improvements to our current training regime that are possible, e.g. using appropriate constraints in the loss function [18] to reduce global non-physical sources of moisture and mass. Finally, coupling to other components (ocean, sea-ice, land) of the climate system is necessary. Tackling these challenges is an exciting opportunity for the growing field of machine learning based climate modeling.

Acknowledgments and Disclosure of Funding

References

[1] Tom Beucler, Pierre Gentine, Janni Yuval, Ankitesh Gupta, Liran Peng, Jerry Lin, Sung-duk Yu, Stephan Rasp, Fiaz Ahmed, Paul A. O'Gorman, J. David Neelin, Nicholas J. Lutsko, and Michael Pritchard. Climate-invariant machine learning. *arXiv*, 2021. doi:10.48550/ARXIV.2112.08440.

[2] Kaifeng Bi, Lingxi Xie, Hengheng Zhang, Xin Chen, Xiaotao Gu, and Qi Tian. Accurate medium-range global weather forecasting with 3d neural networks. *Nature*, 619(7970):533–538, July 2023. doi:10.1038/s41586-023-06185-3.

[3] Boris Bonev, Thorsten Kurth, Christian Hundt, Jaideep Pathak, Maximilian Baust, Karthik Kashinath, and Anima Anandkumar. Spherical fourier neural operators: Learning stable dynamics on the sphere. *Proceedings of the 40th International Conference on Machine Learning (ICML)*, 2023. doi:10.48550/ARXIV.2306.03838.

[4] Christopher S. Bretherton, Brian Henn, Anna Kwa, Noah D. Brenowitz, Oliver Watt-Meyer, Jeremy McGibbon, W. Andre Perkins, Spencer K. Clark, and Lucas Harris. Correcting coarse-grid weather and climate models by machine learning from global storm-resolving simulations. *Journal of Advances in Modeling Earth Systems*, 14(2), February 2022. doi:10.1029/2021ms002794.

[5] Kang Chen, Tao Han, Junchao Gong, Lei Bai, Fenghua Ling, Jing-Jia Luo, Xi Chen, Leiming Ma, Tianning Zhang, Rui Su, Yuanzheng Ci, Bin Li, Xiaokang Yang, and Wanli Ouyang. Fengwu: Pushing the skillful global medium-range weather forecast beyond 10 days lead. *arXiv*, 2023. doi:10.48550/ARXIV.2304.02948.

[6] Spencer K. Clark, Noah D. Brenowitz, Brian Henn, Anna Kwa, Jeremy McGibbon, W. Andre Perkins, Oliver Watt-Meyer, Christopher S. Bretherton, and Lucas M. Harris. Correcting a 200 km resolution climate model in multiple climates by machine learning from 25 km resolution simulations. *Journal of Advances in Modeling Earth Systems*, 14(9), September 2022. doi:10.1029/2022ms003219.

[7] William Collins, Philip Rasch, Byron Boville, James McCaa, David Williamson, Jeffrey Kiehl, Bruce Briegleb, Cecilia Bitz, S.-J. Lin, Minghua Zhang, and Youngjiu Dai. Description of the NCAR Community Atmosphere Model (CAM 3.0). Technical report, UCAR/NCAR, 2004.

[8] Veronika Eyring, Sandrine Bony, Gerald A. Meehl, Catherine A. Senior, Bjorn Stevens, Ronald J. Stouffer, and Karl E. Taylor. Overview of the coupled model intercomparison project phase 6 (CMIP6) experimental design and organization. *Geoscientific Model Development*, 9(5): 1937–1958, May 2016. doi:10.5194/gmd-9-1937-2016.

[9] Yoo-Geun Ham, Jeong-Hwan Kim, and Jing-Jia Luo. Deep learning for multi-year ENSO forecasts. *Nature*, 573(7775):568–572, September 2019. doi:10.1038/s41586-019-1559-7.

[10] Hans Hersbach, Bill Bell, Paul Berrisford, Shoji Hirahara, András Horányi, Joaquín Muñoz-Sabater, Julien Nicolas, Carole Peubey, Raluca Radu, Dinand Schepers, Adrian Simmons, Cornel Soci, Saleh Abdalla, Xavier Abellan, Gianpaolo Balsamo, Peter Bechtold, Gionata Biavati, Jean Bidlot, Massimo Bonavita, Giovanna Chiara, Per Dahlgren, Dick Dee, Michail Diamantakis, Rossana Dragani, Johannes Flemming, Richard Forbes, Manuel Fuentes, Alan Geer, Leo Haimberger, Sean Healy, Robin J. Hogan, Elías Hólm, Marta Janisková, Sarah Keeley, Patrick Laloyaux, Philippe Lopez, Cristina Lupu, Gabor Radnoti, Patricia Rosnay, Iryna Rozum, Freja Vamborg, Sebastien Villaume, and Jean-Noël Thépaut. The ERA5 global reanalysis. *Quarterly Journal of the Royal Meteorological Society*, 146(730):1999–2049, June 2020. doi:10.1002/qj.3803.

[11] Ryan Keisler. Forecasting global weather with graph neural networks. *arXiv*, 2022. doi:10.48550/ARXIV.2202.07575.

[12] Fred Kucharski, Franco Molteni, Martin P. King, Riccardo Farneti, In-Sik Kang, and Laura Feudale. On the need of intermediate complexity general circulation models: A "SPEEDY" example. *Bulletin of the American Meteorological Society*, 94(1):25–30, January 2013. doi:10.1175/bams-d-11-00238.1.

[13] Remi Lam, Alvaro Sanchez-Gonzalez, Matthew Willson, Peter Wirnsberger, Meire Fortunato, Ferran Alet, Suman Ravuri, Timo Ewalds, Zach Eaton-Rosen, Weihua Hu, Alexander Merose, Stephan Hoyer, George Holland, Oriol Vinyals, Jacklynn Stott, Alexander Pritzel, Shakir Mohamed, and Peter Battaglia. Graphcast: Learning skillful medium-range global weather forecasting. *arXiv*, 2022. doi:10.48550/ARXIV.2212.12794.

[14] Zongyi Li, Daniel Zhengyu Huang, Burigede Liu, and Anima Anandkumar. Fourier neural operator with learned deformations for pdes on general geometries. *arXiv*, 2022. doi:10.48550/arXiv.2207.05209.

[15] Tung Nguyen, Johannes Brandstetter, Ashish Kapoor, Jayesh K. Gupta, and Aditya Grover. Climax: A foundation model for weather and climate. *arXiv*, 2023. doi:10.48550/ARXIV.2301.10343.

[16] Jaideep Pathak, Shashank Subramanian, Peter Harrington, Sanjeev Raja, Ashesh Chattopadhyay, Morteza Mardani, Thorsten Kurth, David Hall, Zongyi Li, Kamyar Azizzadenesheli, Pedram Hassanzadeh, Karthik Kashinath, and Animashree Anandkumar. Fourcastnet: A global data-driven high-resolution weather model using adaptive fourier neural operators. *arXiv*, 2022. doi:10.48550/ARXIV.2202.11214.

[17] William M. Putman and Shian-Jiann Lin. Finite-volume transport on various cubed-sphere grids. *Journal of Computational Physics*, 227(1):55–78, November 2007. doi:10.1016/j.jcp.2007.07.022.

[18] M. Raissi, P. Perdikaris, and G.E. Karniadakis. Physics-informed neural networks: A deep learning framework for solving forward and inverse problems involving nonlinear partial differential equations. *Journal of Computational Physics*, 378:686–707, February 2019. doi:10.1016/j.jcp.2018.10.045.

[19] Kevin E. Trenberth, John T. Fasullo, and Jessica Mackaro. Atmospheric moisture transports from ocean to land and global energy flows in reanalyses. *Journal of Climate*, 24(18):4907–4924, September 2011. doi:10.1175/2011jcli4171.1.

[20] UFS Community. Unified forecast system (UFS). *UFS*, Oct 2020. doi:10.5281/zenodo.4460292.

[21] Warren M. Washington and Claire L. Parkinson. *An Introduction to Three-Dimensional Climate Modeling*. University Science Books, Sausalito, CA, 2005.

[22] D. Watson-Parris, Y. Rao, D. Olivié, Ø. Seland, P. Nowack, G. Camps-Valls, P. Stier, S. Bouabid, M. Dewey, E. Fons, J. Gonzalez, P. Harder, K. Jeggle, J. Lenhardt, P. Manshausen, M. Novitasari, L. Ricard, and C. Roesch. ClimateBench v1.0: A benchmark for data-driven climate projections. *Journal of Advances in Modeling Earth Systems*, 14(10), October 2022. doi:10.1029/2021ms002954.

[23] Jonathan A. Weyn, Dale R. Durran, and Rich Caruana. Improving data-driven global weather prediction using deep convolutional neural networks on a cubed sphere. *Journal of Advances in Modeling Earth Systems*, 12(9), September 2020. doi:10.1029/2020ms002109.

[24] Linjiong Zhou, Shian-Jiann Lin, Jan-Huey Chen, Lucas M. Harris, Xi Chen, and Shannon L. Rees. Toward convective-scale prediction within the next generation global prediction system. *Bulletin of the American Meteorological Society*, 100(7):1225 – 1243, 2019. doi:https://doi.org/10.1175/BAMS-D-17-0246.1.

Table 1: Input and output variables for ACE. The k subscript refers to a vertical layer index, and ranges from 0 to 7 starting at the top of atmosphere and increasing towards the surface. The Time column indicates whether a variable represents the value at a particular time step ("Snapshot"), the average across the 6-hour time step ("Mean") or a quantity which does not depend on time ("Invariant"). "TOA" denotes "Top Of Atmosphere", the climate model's upper boundary.

Prognostic (input and output)			
Symbol	Description	Units	Time
T_k	Air temperature	K	Snapshot
q_k^T	Specific total water (vapor + condensates)	kg/kg	Snapshot
u_k	Windspeed in eastward direction	m/s	Snapshot
v_k	Windspeed in northward direction	m/s	Snapshot
T_s	Skin temperature of land or sea-ice	K	Snapshot
p_s	Atmospheric pressure at surface	Pa	Snapshot
Forcing (input only)			
Symbol	Description	Units	Time
$DSWRFtoa$	Downward shortwave radiative flux at TOA	W/m^2	Mean
T_s	Skin temperature of open ocean	K	Snapshot
z_s	Surface height of topography	m	Invariant
f_l	Land grid cell fraction	—	Invariant
f_o	Ocean grid cell fraction	—	Snapshot
f_{si}	Sea-ice grid cell fraction	—	Snapshot
Diagnostic (output only)			
Symbol	Description	Units	Time
$USWRFtoa$	Upward shortwave radiative flux at TOA	W/m^2	Mean
$ULWRFtoa$	Upward longwave radiative flux at TOA	W/m^2	Mean
$USWRFsfc$	Upward shortwave radiative flux at surface	W/m^2	Mean
$ULWRFsfc$	Upward longwave radiative flux at surface	W/m^2	Mean
$DSWRFsfc$	Downward shortwave radiative flux at surface	W/m^2	Mean
$DLWRFsfc$	Downward longwave radiative flux at surface	W/m^2	Mean
P	Surface precipitation rate (all phases)	kg/m^2/s	Mean
$\frac{\partial TWP}{\partial t}\big|_{adv}$	Tendency of total water path from advection	kg/m^2/s	Mean
LHF	Surface latent heat flux	W/m^2	Mean
SHF	Surface sensible heat flux	W/m^2	Mean

A   Data preprocessing

The complete list of input and output variables used for ACE is given in Table 1. A schematic depiction of the meaning of forcing, prognostic and diagnostic variables is shown in Figure 5.

Horizontal regridding   FV3GFS, the model used to generate reference data, uses a cubed sphere grid [17]. This grid prevents direct use of the SFNO architecture, which in the formulation of [3] requires data on a latitude-longitude grid. Therefore, we regrid to latitude-longitude using the "fregrid" tool provided by NOAA GFDL. We use the first-order conservative regridding option. This regridding procedure leads to unphysical sharp gradients in the high latitudes for some fields. Therefore as part of the regridding process, we also perform a round-trip with the spherical harmonic transform which has the effect of filtering out these unrealistic artifacts. For the 2x coarser FV3GFS baseline, regridding to the 100km latitude-longitude grid upsampled the dataset from its native resolution and produced more profound artifacts, and so when performing the spherical harmonic transform round-trip on this dataset we truncated the highest-frequency modes (35% of all modes), which had the effect of reducing the baseline's errors against the reference dataset.

In future work, it would be natural to directly train on the cubed sphere grid data, which would prevent complications associated with regridding. The cubed sphere grid has been used for ML-
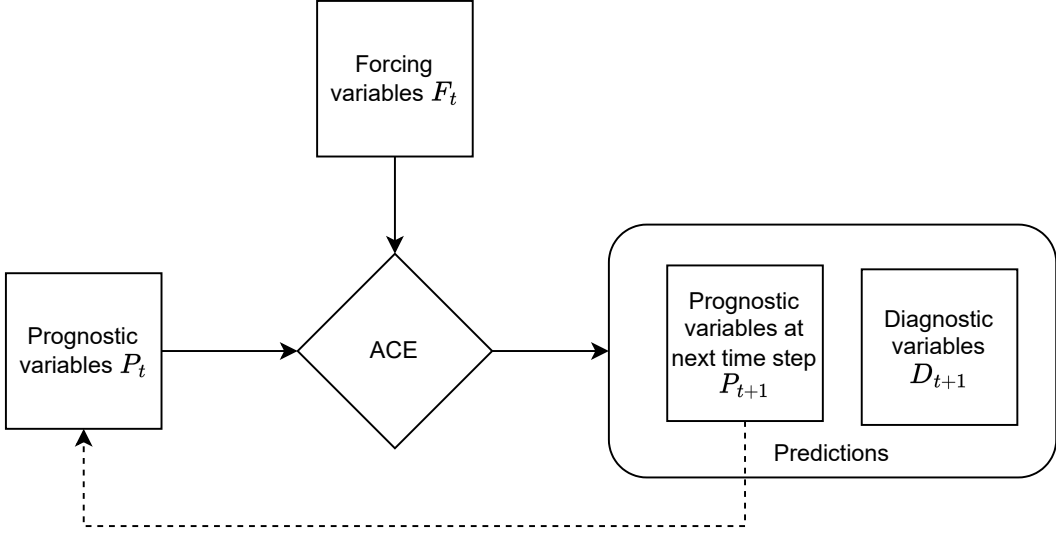
Figure 5: Diagram summarizing the flow of input and output variables. Prognostic variables are fed back into the model autoregressively. Forcing variables are read from an external dataset and appended to the prognostic variables at each step. The network outputs diagnostic variables, which contribute to the loss but are not passed back as inputs for the next step.

based weather prediction architectures [23] and adaptations of Fourier Neural Operators for arbitrary geometric discretizations have been proven in low dimensional settings that could be readily extended to SFNO [14].

Vertical coarse-graining   After the horizontal regridding is done for all variables, anticipating the requirements for precise mass and energy conservation, we vertically integrate the 3D variables (air temperature, specific total water, eastward wind and northward wind) from the original 63 vertical layers to 8 layers. The reference model FV3GFS uses a hybrid sigma-pressure vertical coordinate (e.g. Figure 3.1 of [7]) where the pressure at vertical layer interface k is defined by:

$$p_k = a_k + b_k p_s \tag{2}$$

where a_k and b_k are constant coefficients and p_s is the surface pressure. We also use a hybrid sigma-pressure vertical coordinate for ACE, but subselect the a_k and b_k coordinates from FV3GFS to nine interfaces (Table 2) corresponding to eight finite volume vertical layers. The nine interfaces were chosen to have a vertical coordinate that corresponds closely to the one in the SPEEDY model [12]. The uppermost two layers correspond to the stratosphere while the lowermost layer is roughly a boundary layer average. The following equation, using temperature T as an example, is used to transform all 3D variables from the 63-layer to 8-layer vertical coordinate:

$$\overline{T}_k = \frac{1}{\overline{dp_k}} \sum_{i=I_k}^{I_{k+1}} T_i \, dp_i \tag{3}$$

where

$$\overline{dp}_k = \sum_{i=I_k}^{I_{k+1}} dp_i \tag{4}$$

and dp_i and T_i are the pressure thickness and temperature of the i'th atmospheric layer in the original vertical coordinate and I_k is the index of the original vertical coordinate (fourth column of Table 2). The pressure thickness $dp_i = p_{i+1} - p_i$ is computed by taking the difference between the vertical interface pressures given by Equation 2. The use of this finite volume vertical coordinate ensures that exact vertical integrals of quantities such as mass, moisture and energy can be computed and expected to balance with fluxes into and out of the atmosphere.

9

Table 2: ACE vertical coordinate. Here k indicates the vertical layer interface ranging from the top of the model's atmosphere $k = 0$ to the Earth surface $k = 8$. a_k and b_k define the vertical coordinate (Equation 2) while I_k indicates what the corresponding vertical index is in the 63-layer reference FV3GFS simulation. p_k^{ref} is the pressure at model layer interfaces assuming $p_s = 1000$hPa.

k	a_k [Pa]	b_k [unitless]	I_k	p_k^{ref} [hPa]
0	64.247	0.0	0	0.642
1	5167.14603	0.0	18	51.7
2	12905.42546	0.01755	26	147
3	13982.4677	0.11746	31	257
4	12165.28766	0.2896	36	411
5	8910.07678	0.49806	41	587
6	4955.72632	0.72625	47	776
7	2155.78385	0.88192	53	903
8	0.0	1.0	63	1000

Table 3: SFNO hyperparameters. Names correspond to the definition of the Spherical-FourierNeuralOperatorNet class found here: https://github.com/ai2cm/modulus/blob/94f62e1ce2083640829ec12d80b00619c40a47f8/modulus/models/sfno/sfnonet.py#L292. All configuration options not listed here are set to the defaults at the linked code.

Name	Value
embed_dim	256
filter_type	linear
num_layers	8
operator_type	dhconv
scale_factor	1
spectral_layers	3

B Hyperparameters

Table 3 lists the SFNO hyperparameters used in this study. See [3] for details about the meaning of these parameters. The only modification to the architecture of SFNO made in this work is in the first spherical harmonic transform and the last inverse spherical harmonic transform, where Gauss-Legendre quadrature is used, as our data is on the Gaussian grid as opposed to the equiangular latitude-longitude grid used in [3] (see horizontal regridding section of Appendix A).

Table 4 lists the hyperparameters used for optimization. Model parameters were averaged across training step using an exponential moving average (EMA), which led to moderate (up to 15%) improvements in the time-mean RMSE metric.

C Metrics

Suppose we have an arbitrary predicted field $\hat{x}(t, \phi, \lambda)$ which depends on time t, latitude ϕ and longitude λ and its corresponding target/ground truth $x(t, \phi, \lambda)$. Let $A(\phi, \lambda)$ be a normalized weight

Table 4: Optimization hyperparameters.

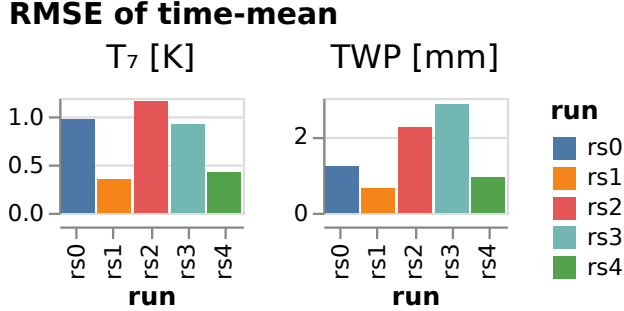| Name	Value
Optimizer	Adam
Initial learning rate	1×10^{-4}
Learning rate schedule	Cosine annealing (single cycle)
Number of epochs	30
Batch size	4
Exponential moving average decay rate	0.9999

RMSE of time-mean

Figure 6: Time-mean RMSE (Equation 6) of T_7 and $\text{TWP} = \frac{1}{g} \sum_k q_k^T \, dp_k$ computed over a single 10-year inference for five ML models which differ only in initialization random seed.

proportional to the area of a grid cell. Then the three metrics of interest are:

$$GM_{\hat{x}}(t) = \sum_{\phi,\lambda} A(\phi,\lambda) \hat{x}(t,\phi,\lambda) \tag{5}$$

$$RMSE\text{-}TM_{\hat{x}} = \sqrt{\sum_{\phi,\lambda} A(\phi,\lambda) \left[\underset{t}{\text{mean}} \left\{ \hat{x}(t,\phi,\lambda) - x(t,\phi,\lambda) \right\} \right]^2} \tag{6}$$

$$GM\text{-}TM\text{-}BIAS_{\hat{x}} = \underset{t}{\text{mean}} \left[GM_{\hat{x}}(t) - GM_x(t) \right] \tag{7}$$

D Random seed ensemble

Figure 6 shows the time-mean RMSE across a 5-member random seed ensemble of models. Although all models are capable of stable 10-year inference runs, the magnitude of the time-mean RMSE metric can vary by up to a factor 4 (depending on output variable being considered). The results in the main body of the paper are all based on the "rs1" model which has lowest errors for T_7 and total water path. We have verified that the spread in error across different initial conditions is significantly smaller than the spread across random seeds for a single initial condition (not shown).

E Systematic evaluation of all outputs

In this section we provide a complete description of the global climate biases of ACE relative to the baseline and reference. Figure 7 shows the magnitude of the time-mean pattern errors (Equation 6) for each output variable except the total water path advective tendency which was not available for the baseline run. Out of the 44 output variables, an impressive 41 have lower RMSE for ACE when compared to the baseline.

Figure 8 shows the time- and global-mean bias (Equation 7) for all output channels. In general biases are low for all variables (e.g. radiative flux biases are at most 1.2 W/m^2) but they are mostly larger compared to the baseline simulation. In particular the approximately -25 Pa p_s bias is large compared to the near-zero bias in the baseline simulation which exactly conserves global dry air mass and moisture.

Figure 9 shows the timeseries of the global mean for all output variables. Most variables track the global-mean season cycle well and none have large drifts that persist throughout the 10-year simulation. Nevertheless, there are deviations from the expected global mean that are larger than interannual variability (specifically in p_s, q_0^T and a number of the northward wind v_k variables).

F 100-year forecasts

Since our forcing dataset is annually repeating, it is straightforward to repeat it in order to allow arbitrarily long forecasts. We used this feature to do a 100-year long forecast. The forecast was stable
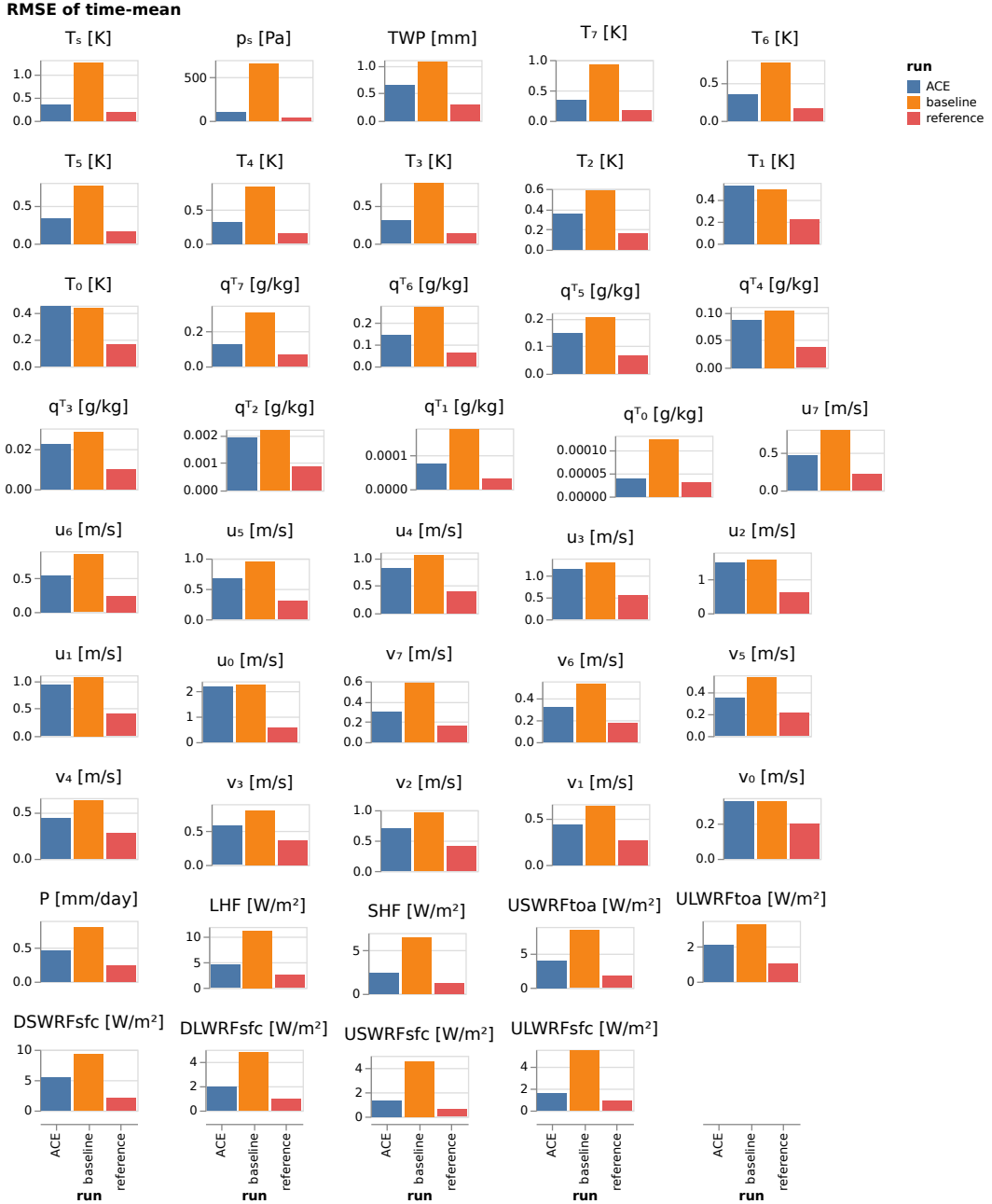
Figure 7: The RMSE of the time-mean (Equation 6) of all output variables for ACE, the coarser resolution baseline and the reference simulation.
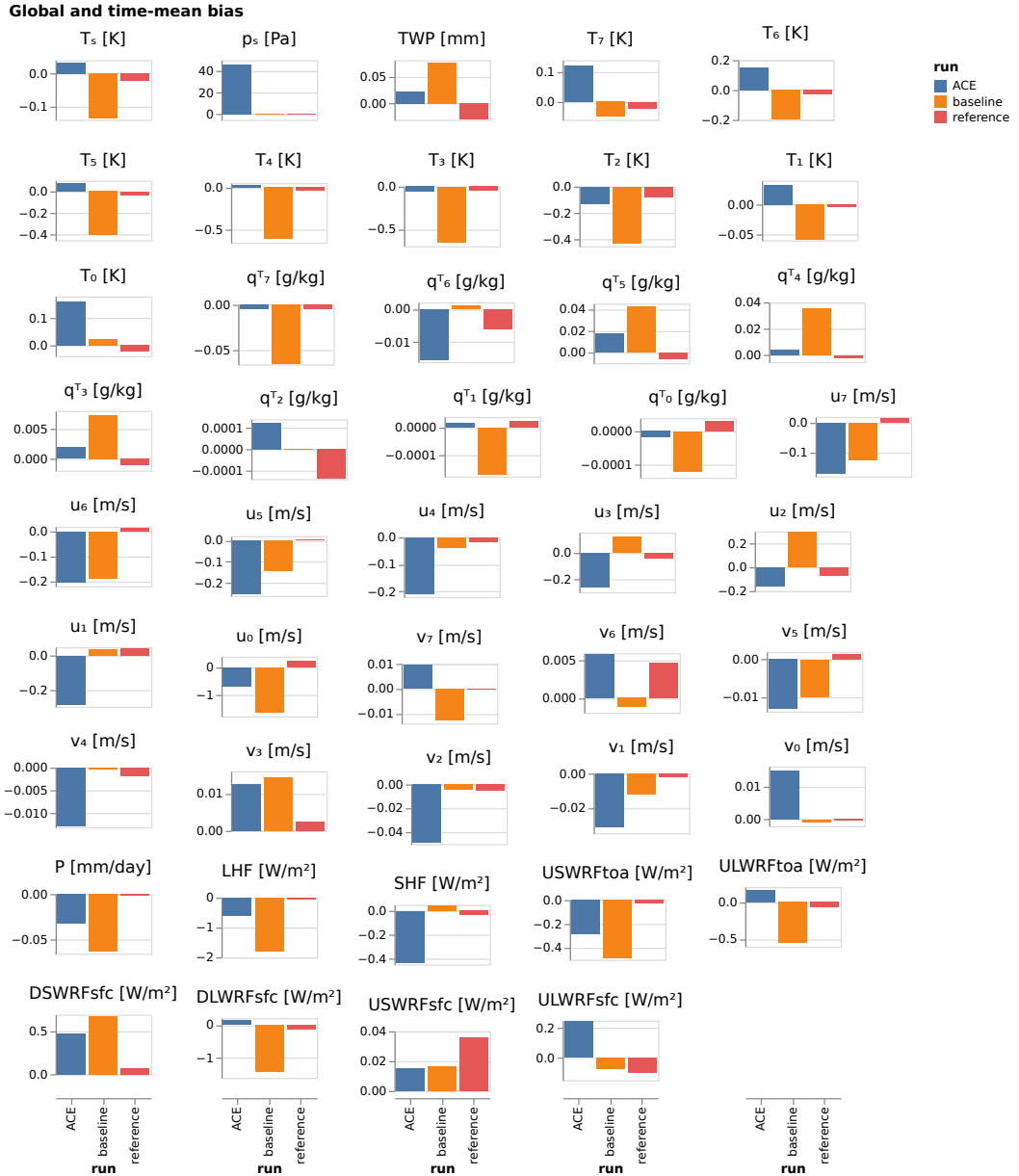
Figure 8: The global- and time-mean bias (Equation 7) of all output variables for ACE, the coarser resolution baseline and the reference simulation.
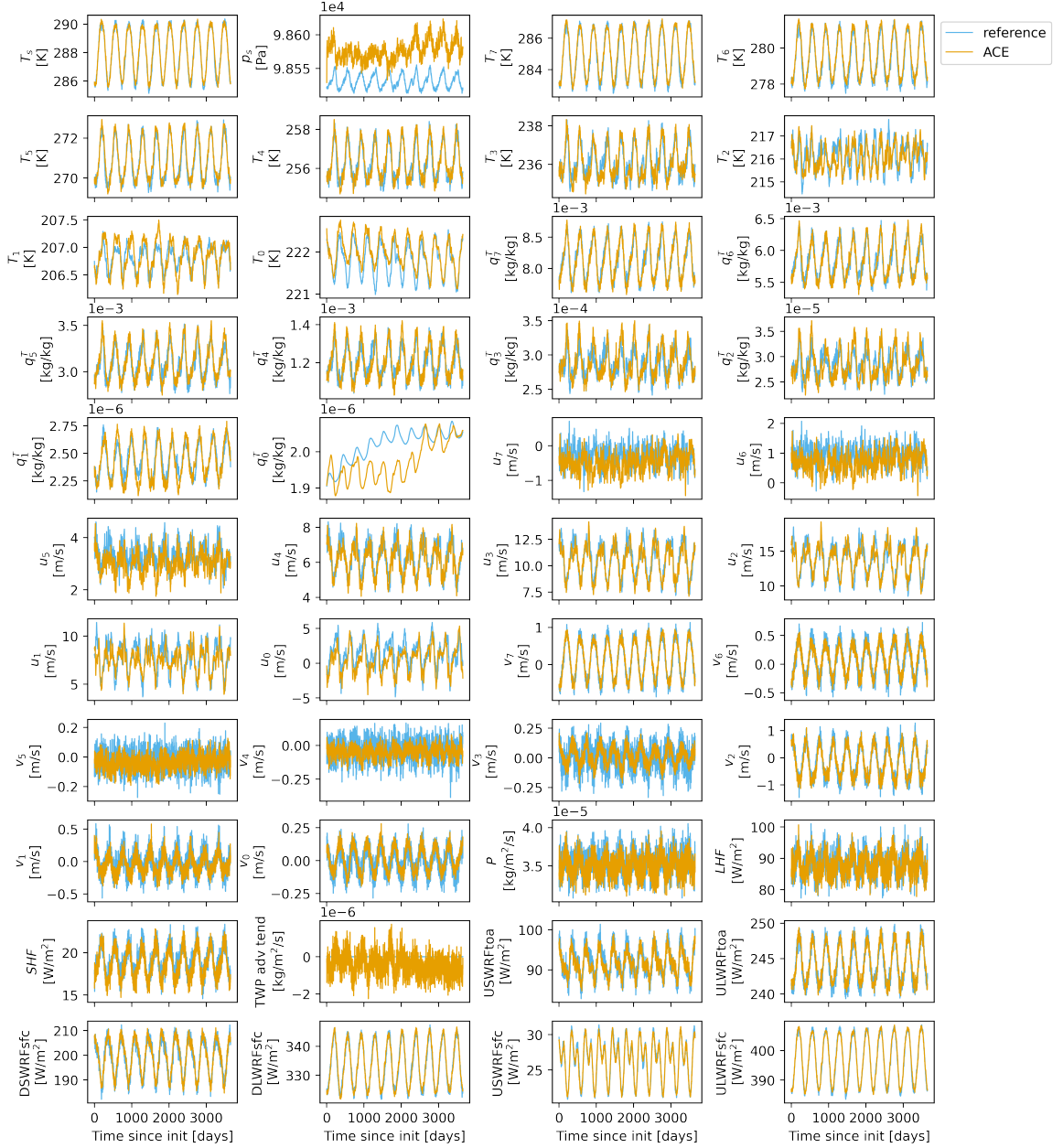
Figure 9: The daily averaged global mean (Equation 5) of all output variables for ACE and the reference simulation.
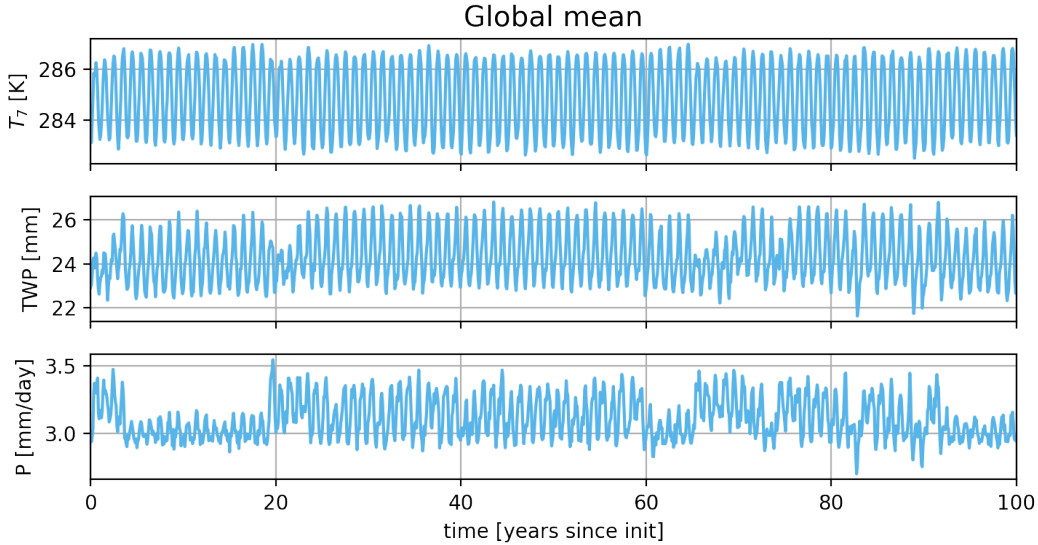
Figure 10: Timeseries of monthly-mean and global-mean (top) T_7, (middle) total water path and (bottom) surface precipitation rate P from 100-year forecast.

and no variables showed long-term drifts. However, there are some unrealistic fluctuations on annual timescales, for example for global mean surface precipitation rate (bottom row of Figure 10).

G Global mean conservation

The last paragraph of Section 3 discussed the column budget of moisture and showed that ACE nearly conserves column moisture for individual timesteps. Here we compute the area-weighted global mean of Equation 1 and show the global budget violation (left-hand side of Equation 1 minus right-hand side of Equation 1) in the left panel of Figure 11. Although for most of the simulation the violation is not overly large (magnitude less than 0.1 mm/day; compared to typical values of global mean precipitation or evaporation of 3 mm/day) at certain times in the simulation the global budget violation is up to magnitude 0.4 mm/day.

We also consider the conservation of global dry air mass. Surface pressure due to dry air only is

$$p_s^{dry} = p_s - g \cdot TWP. \tag{8}$$

On the timescales we are considering, there is no flux of dry air mass through the top of atmosphere or through the Earth's surface. Therefore, the global mean surface pressure due to dry air should remain exactly constant. Indeed this is the case for the reference model. The right panel of Figure 11 shows slight deviations for ACE of magnitude up to 150 Pa, but no systematic multi-year drift.

It is possible that adding terms to the loss function to encourage global mean conservation of moisture and dry air mass [18] would improve these characteristics for long simulations.

H Normalization Strategy

This section describes the "residual" scaling strategy and compares it to the "full-field" normalization done in [16]. First the standard scaling mean and standard deviations are computed over time, latitude and longitude, without area weighting:

$$\mu(a) = \underset{t,\phi,\lambda}{\text{mean}}\, a(t, \phi, \lambda) \tag{9}$$

$$\sigma(a) = \underset{t,\phi,\lambda}{\text{std}}\, a(t, \phi, \lambda). \tag{10}$$

The "full-field" normalization (as in [16]) is defined as $a_{ff} = (a - \mu(a))/\sigma(a)$. Some prognostic variables, for example surface pressure p_s, vary more strongly over space than over time, so their
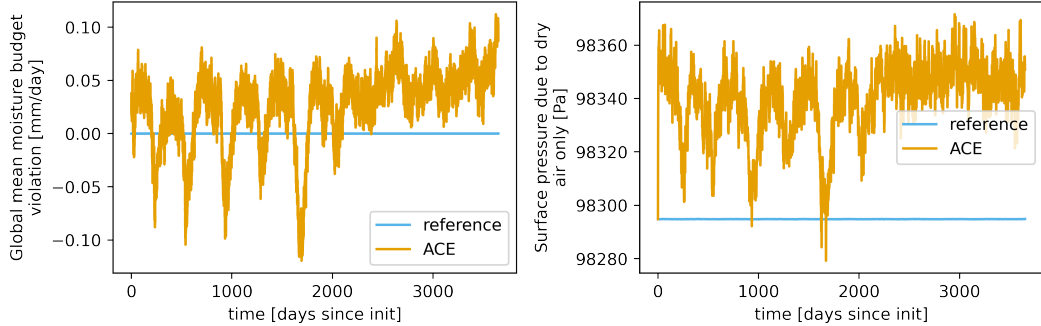
15

Figure 11: Left: timeseries of the global mean moisture budget violation (LHS minus RHS of Equation 1). Right: timeseries of global mean surface pressure due to dry air only (Equation 8).

normalized timestep-to-timestep differences $a'_{ff} = a_{ff}(t+1) - a_{ff}(t)$ (which is what we'd really like to get right for each prognostic variable) vary strongly between variables. It is cumbersome to change the loss function in FourCastNet to reflect this goal. As a pragmatic substitute, we modify the normalization strategy to give equal contributions from tendency errors in each variable to the loss function (see also Section 3.3.3 of [11] which normalized the loss with a similar motivation). First we compute the forward increment of the normalized variables as:

$$a'_{ff}(t) = a_{ff}(t+1) - a_{ff}(t). \tag{11}$$

Define $\sigma(a'_{ff})$ is the standard deviation of a'_{ff}. Neglecting any temporal trend in a_{ff} across the training period, $\mu(a'_{ff}) = 0$, so

$$\sigma^2(a'_{ff}) = \frac{1}{TXY} \sum_{t,x,y} (a'_{ff})^2 \tag{12}$$

We rescale the full-field-normalized variables as follows:

$$a_{res} = a_{ff}/\sigma_{res}(a) \tag{13}$$

$$\sigma_{res}(a) = \sigma(a'_{ff})/\overline{\sigma(a'_{ff})}^g \tag{14}$$

This "residual" rescaling includes a factor $\overline{\sigma(a'_{ff})}^g$, the geometric mean of $\sigma(a'_{ff})$ across all variables, so that the standard deviations of the rescaled variables stay scattered about 1.

Figure 12 shows the "residual" rescaling factors $\sigma_{res}(a)$ of all variables a. The range is about a factor of 30, with the surface pressure being up-weighted the most relative to the "full field" normalization. Residual normalization is more justifiable for prognostic variables (which are both inputs and outputs) than for diagnostic variables. Hence, we attempted to apply residual scaling only to prognostic variables, but this leads to slightly larger time-mean biases than also rescaling diagnostic variables.

I Ablations

I.1 Normalization

Note that neither of the models used in this ablation (Figure 13) have the same configuration as the for the results shown in the main body of the manuscript. In particular, neither of them use the surface type fractions as inputs.

To show the impact of the "residual scaling" normalization choice described in Appendix H, Figure 13 shows the 1-step validation RMSE, 5-day RMSE and time-mean RMSE ($RMSE\text{-}TM_{p_s}$) of surface pressure and 5-day RMSE of USWRFtoa as a function of training steps. Not surprisingly since we are weighting it more strongly, a large (about 50%) decrease in 1-step RMSE is seen for p_s. We also see a large improvement for 5-day RMSE, and smaller improvement for time-mean RMSE of p_s. Notably, even though the USWRFtoa variable is weighted less heavily in the loss function (see Figure 12) its 5-day RMSE is substantially improved with residual scaling. We believe this is because the improved autoregressive performance of p_s leads to more accurate predictions for other variables also.
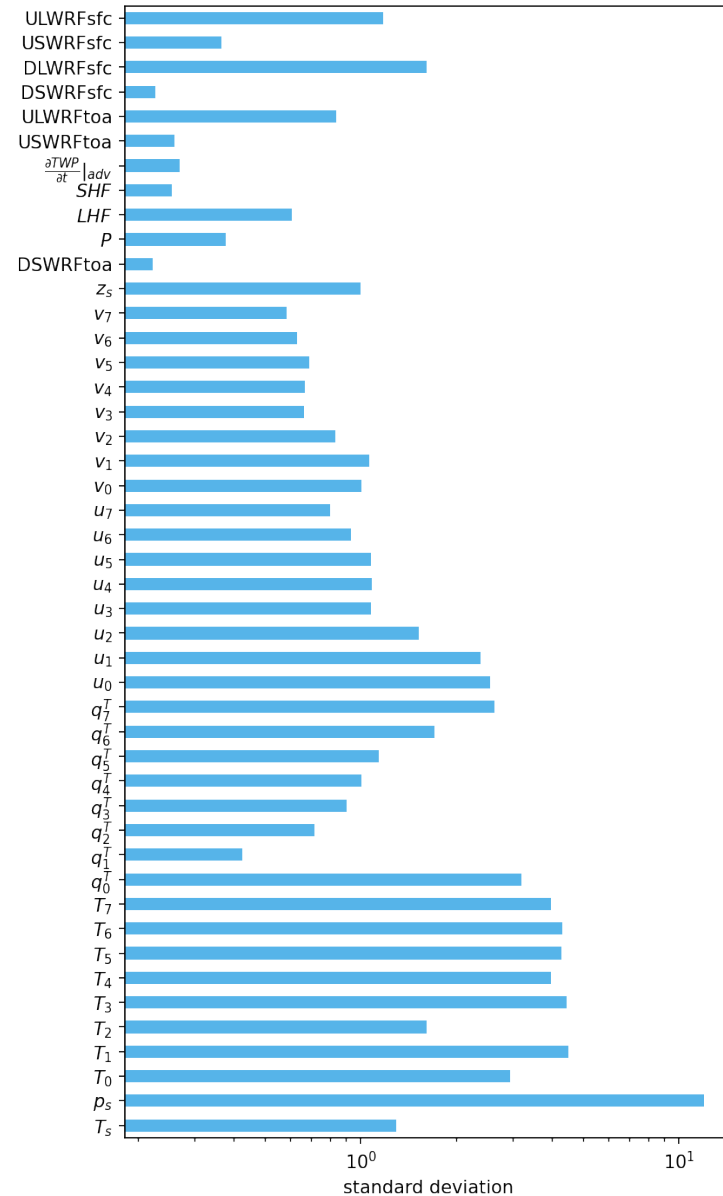
16

Figure 12: The standard deviation of normalized variables using the "residual" scaling strategy. Table 1 gives meaning of each variable.
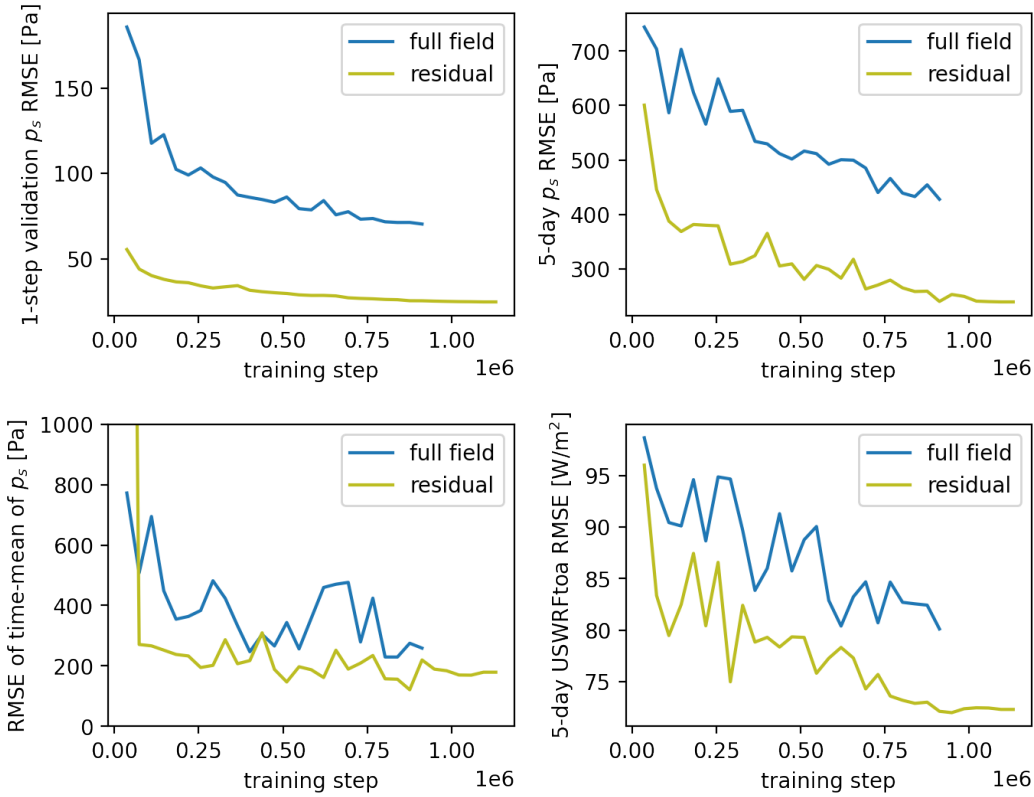
Figure 13: Four metrics evaluated on models which use (blue) full field normalization and (olive) residual normalization, shown as a function of training step and reported once per epoch. The metrics are (top-left) RMSE of 1-step p_s prediction on validation data, (top-right) RMSE of p_s after 5 days of autoregressive inference, (bottom-left) RMSE of time-mean p_s over 1-year simulation and (bottom-right) RMSE of USWRFtoa after 5 days of autoregressive inference.

I.2 Dataset size

To show importance of dataset, here we compare training curves for two experiments which are similarly configured. The only difference is that the first uses a dataset with 10-years of training data (14607 samples; a single member of the 10-member ensemble of reference simulations) and trains for 75 epochs while the second uses a 100-year dataset (146070 samples) and trains for 15 epochs. Note the latter training is not the same as the one described in the main text above. It does not use surface height or surface type fractions as inputs and it uses a 5x larger initial learning rate.

Figure 14 shows the training and validation loss for the models trained on the two datasets. The validation loss here is computed on 80 samples from the independent validation dataset. The model trained on only 10 years of data shows clear signs of overfitting that does not occur for the 100-year dataset.

When examining the variable-by-variable validation RMSE, we find that only stratospheric variables overfit for the 10-year dataset. As an example, Figure 15 compares the validation RMSE for the upper stratospheric T_0 and the near-surface T_7. This makes it apparent that the overfitting is happening for temperature in the stratosphere. This is also the case for other stratospheric variables T_1, v_0, u_0, q_0^T and q_1^T (not shown). Given that stratospheric dynamics are typically slower than variability in the troposphere, it is not a surprise that overfitting is a particular concern in the uppermost model layers. Interestingly, ML-based weather prediction systems have reported relatively poor performance in the stratosphere (e.g. Fig. 2 of [13]).
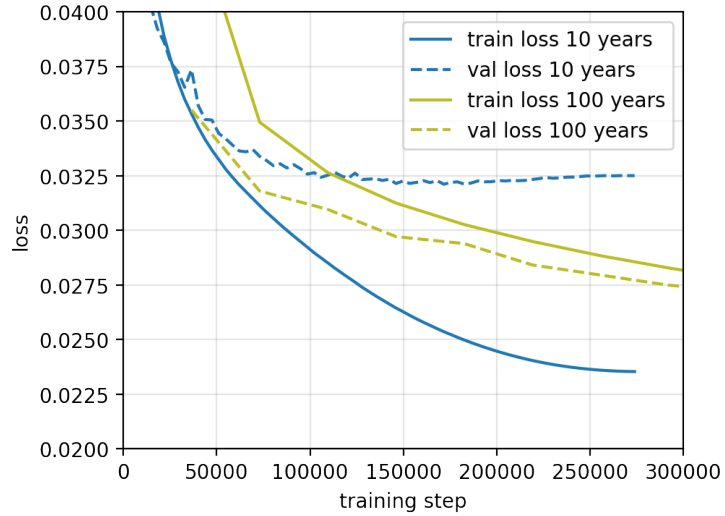
Figure 14: The (solid) train loss and (dashed) validation loss for training runs on (blue) a 10-year dataset and (olive) a 100-year dataset.
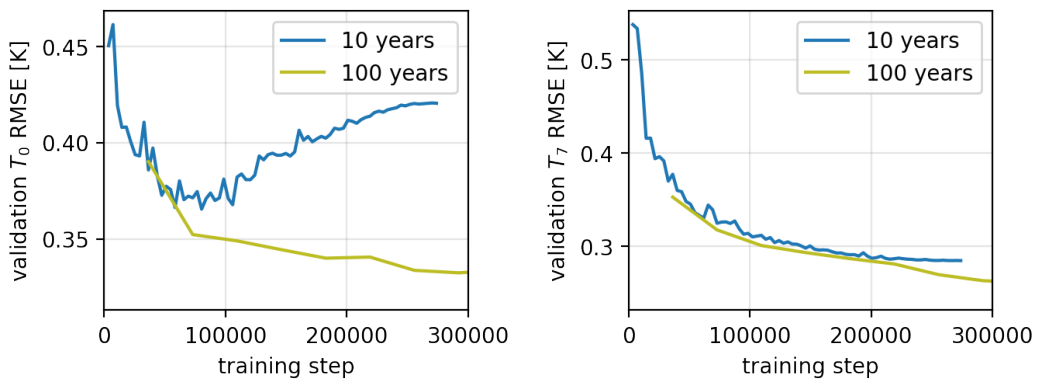

Figure 15: The validation RMSE of (left) T_0 and (right) T_7 for models trained on (blue) a 10-year dataset and (olive) a 100-year dataset.